# Quantitative imaging using high-energy X-ray phase-contrast CT with a 70 kVp polychromatic X-ray spectrum

**Adrian Sarapata,[1,*] Marian Willner,[1] Marco Walter,[2] Thomas Duttenhofer,[2] Konradin Kaiser,[2] Pascal Meyer,[3] Christian Braun,[4] Alexander Fingerle,[5] Peter B. Noël,[5] Franz Pfeiffer,[1] and Julia Herzen[1]**

[1]*Lehrstuhl für Biomedizinische Physik, Physik-Department & Institut für Medizintechnik, Technische Universität München, 85748 Garching, Germany*
[2]*Microworks GmbH, 76137 Karlsruhe, Germany*
[3]*Karlsruhe Institute of Technology, 76344 Eggenstein-Leopoldshafen, Germany*
[4]*Institute of Forensic Medicine, Ludwig-Maximilians-Universität, 81675 Munich, Germany*
[5]*Department of Radiology, Technische Universität München, 81675 Munich, Germany*
[*]*adrian.sarapata@tum.de*

**Abstract:** Imaging of large and dense objects with grating-based X-ray phase-contrast computed tomography requires high X-ray photon energy and large fields of view. It has become increasingly possible due to the improvements in the grating manufacturing processes. Using a high-energy X-ray phase-contrast CT setup with a large (10 cm in diameter) analyzer grating and operated at an acceleration tube voltage of 70 kVp, we investigate the complementarity of both attenuation and phase contrast modalities with materials of various atomic numbers (Z). We confirm experimentally that for low-Z materials, phase contrast yields no additional information content over attenuation images, yet it provides increased contrast-to-noise ratios (CNRs). The complementarity of both signals can be seen again with increasing Z of the materials and a more comprehensive material characterization is thus possible. Imaging of a part of a human cervical spine with intervertebral discs surrounded by bones and various soft tissue types showcases the benefit of high-energy X-ray phase-contrast system. Phase-contrast reconstruction reveals the internal structure of the discs and makes the boundary between the disc annulus and nucleus pulposus visible. Despite the fact that it still remains challenging to develop a high-energy grating interferometer with a broad polychromatic source with satisfactory optical performance, improved image quality for phase contrast as compared to attenuation contrast can be obtained and new exciting applications foreseen.



**OCIS codes:** (110.7440) X-ray imaging; (110.6955) Tomographic imaging; (110.3175) Interferometric imaging.

## References and links

1. H. Hetterich, M. Willner, S. Fill, J. Herzen, F. Bamberg, A. Hipp, U. Schller, S. Adam-Neumair, S. Wirth, M. Reiser, and et al., "Phase-contrast ct: Qualitative and quantitative evaluation of atherosclerotic carotid artery plaque," Radiology **271**, 870–878 (2014).

#224758 - $15.00 USD Received 13 Oct 2014; revised 25 Nov 2014; accepted 7 Dec 2014; published 9 Jan 2015

2. M. Willner, J. Herzen, S. Grandl, S. Auweter, D. Mayr, A. Hipp, M. Chabior, A. Sarapata, K. Achterhold, I. Zanette, and et al., "Quantitative breast tissue characterization using grating-based x-ray phase-contrast imaging," Phys. Med. Biol. **59**, 1557–1571 (2014).
3. J. Herzen, M. S. Willner, A. A. Fingerle, P. B. Nol, T. Khler, E. Drecoll, E. J. Rummeny, and F. Pfeiffer, "Imaging liver lesions using grating-based phase-contrast computed tomography with bi-lateral filter post-processing," PLoS ONE **9**, e83369 (2014).
4. G. Schulz, A. Morel, M. S. Imholz, H. Deyhle, T. Weitkamp, I. Zanette, F. Pfeiffer, C. David, M. Mller-Gerbl, and B. Mller, "Evaluating the microstructure of human brain tissues using synchrotron radiation-based micro-computed tomography," Proc. SPIE **7804**, 78040F (2010).
5. M. Willner, M. Bech, J. Herzen, I. Zanette, D. Hahn, J. Kenntner, J. Mohr, A. Rack, T. Weitkamp, and F. Pfeiffer, "Quantitative x-ray phase-contrast computed tomography at 82 kev," Opt. Express **21**, 4155–4166 (2013).
6. T. Donath, F. Pfeiffer, O. Bunk, W. Groot, M. Bednarzik, C. Grunzweig, E. Hempel, S. Popescu, M. Hoheisel, and C. David, "Phase-contrast imaging and tomography at 60 kev using a conventional x-ray tube source," Rev. Sci. Instrum. **80**, 053701 (2009).
7. A. Sarapata, J. W. Stayman, M. Finkenthal, J. H. Siewerdsen, F. Pfeiffer, and D. Stutman, "High energy x-ray phase contrast ct using glancing-angle grating interferometers," Med. Phys. **41**, 021904 (2014).
8. T. Thuering, M. Abis, Z. Wang, C. David, and M. Stampanoni, "X-ray phase-contrast imaging at 100 kev on a conventional source," Sci. Rep. **4**, 5198 (2014).
9. J. Herzen, T. Donath, F. Pfeiffer, O. Bunk, C. Padeste, F. Beckmann, A. Schreyer, C. David *et al.*, "Quantitative phase-contrast tomography of a liquid phantom using a conventional x-ray tube source," Opt. Express **17**, 10010–10018 (2009).
10. A. Momose, W. Yashiro, Y. Takeda, Y. Suzuki, and T. Hattori, "Phase tomography by x-ray talbot interferometry for biological imaging," Jpn. J. Appl. Phys. **45**, 5254–5262 (2006).
11. T. Weitkamp, A. Diaz, C. David, F. Pfeiffer, M. Stampanoni, P. Cloetens, and E. Ziegler, "X-ray phase imaging with a grating interferometer," Opt. Express **13**, 6296–6304 (2005).
12. F. Pfeiffer, C. Kottler, O. Bunk, and C. David, "Hard x-ray phase tomography with low-brilliance sources," Phys. Rev. Lett. **98**, 108105 (2007).
13. F. Pfeiffer, T. Weitkamp, O. Bunk, and C. David, "Phase retrieval and differential phase-contrast imaging with low-brilliance x-ray sources," Nature Phys. **2**, 258–261 (2006).
14. E. Reznikova, J. Mohr, M. Boerner, V. Nazmov, and P.-J. Jakobs, "Soft x-ray lithography of high aspect ratio su8 submicron structures," Microsyst. Technol. **14**, 1683–1688 (2008).
15. J. Mohr, T. Grund, D. Kunka, J. Kenntner, J. Leuthold, J. Meiser, J. Schulz, and M. Walter, "High aspect ratio gratings for x-ray phase contrast imaging," AIP Conf. Proc. **1466**, 41–50 (2012).
16. P. Meyer, J. Schulz, and V. Saile, "Deep x-ray lithography," in "Micro-Manufacturing Engineering and Technology," , Y. Qin, ed. (Elsevier, 2010), pp. 202–220.
17. J. Meiser, M. Amberger, M. Willner, D. Kunka, P. Meyer, F. Koch, A. Hipp, M. Walter, F. Pfeiffer, and J. Mohr, "Increasing the field of view of x-ray phase contrast imaging using stitched gratings on low absorbent carriers," Proc. SPIE **9033**, 903355 (2014).
18. A. J. C. Wilson, *The Optical Principles of the Diffraction of X-rays by R.W. James*, vol. III (International Union of Crystallography (IUCr), 1950).
19. R. James, *The optical principles of the diffraction of x-rays*, Crystalline State (Bell, 1967).
20. E. C. McCullough, "Photon attenuation in computed tomography," Med. Phys. **2**, 307–320 (1975).
21. J. H. Hubbell, "Photon cross sections, attenuation coefficients, and energy absorption coefficients from 10 kev to 100 gev," Tech. rep., NSRDS-NBS (1969).
22. M. J. Berger, J. H. Hubbell, S. M. Seltzer, J. Chang, J. S. Coursey, R. Sukumar, D. S. Zucker, and K. Olsen, "XCOM: Photon cross section database," (2010).
23. T. Kohler, K. Jurgen Engel, and E. Roessl, "Noise properties of grating-based x-ray phase contrast computed tomography," Med. Phys. **38**, S106–S116 (2011).
24. T. Donath, M. Chabior, F. Pfeiffer, O. Bunk, E. Reznikova, J. Mohr, E. Hempel, S. Popescu, M. Hoheisel, M. Schuster, and et al., "Inverse geometry for grating-based x-ray phase-contrast imaging," J. Appl. Phys. **106**, 054703 (2009).
25. G. Poludniowski, G. Landry, F. DeBlois, P. M. Evans, and F. Verhaegen, "Spekcalc: a program to calculate photon spectra from tungsten anode x-ray tubes," Phys. Med. Biol. **54**, N433–N438 (2009).
26. F. Pfeiffer, M. Bech, O. Bunk, P. Kraft, E. F. Eikenberry, C. Bronnimann, C. Grnzweig, and C. David, "Hard-x-ray dark-field imaging using a grating interferometer," Nature Mater. **7**, 134–137 (2008).
27. T. Koehler and E. Roessl, "Simultaneous de-noising in phase contrast tomography," AIP Conf. Proc. **1466**, 78–83 (2012).
28. P. Bandyopadhyay and C. Segre, Mucal 1.3, http://www.csrri.iit.edu/mucal.html (April 2009).
29. A. Malecki, G. Potdevin, and F. Pfeiffer, "Quantitative wave-optical numerical analysis of the dark-field signal in grating-based x-ray interferometry," Europhys. Lett. **99**, 48001 (2012).
30. S. J. Matcher, C. P. Winlove, and S. V. Gangnus, "The collagen structure of bovine intervertebral disc studied using polarization-sensitive optical coherence tomography," Phys. Med. Biol. **49**, 1295–1306 (2004).

#224758 - $15.00 USD Received 13 Oct 2014; revised 25 Nov 2014; accepted 7 Dec 2014; published 9 Jan 2015

31. R. Raupach and T. G. Flohr, "Analytical evaluation of the signal and noise propagation in x-ray differential phase-contrast computed tomography," Phys. Med. Biol. **56**, 2219–2244 (2011).
32. D. Stutman and M. Finkenthal, "Glancing angle talbot-lau grating interferometers for phase contrast imaging at high x-ray energy," Appl. Phys. Lett. **101**, 091108 (2012).

## 1. Introduction

Grating-based X-ray phase-contrast computed tomography (PC-CT) is a well established technique providing simultaneously three different contrast mechanisms. The additional information improves detectability of certain features inside the sample and improves differentiation of various materials. The possibility of being operated with conventional X-ray tubes enabled an easier/lower-cost access to the method and opened a wide range of applications, mostly in biomedical imaging.

Because of limitations in the grating fabrication process, the technique has been restricted to X-ray energies below 40 keV and small fields of view (FOVs). Mainly relatively small samples (maximum 30 mm in diameter) composed of low-Z materials have been investigated [1–3]. When larger samples are of interest, asymmetric rotation axis position can be used [4] which works well only with parallel beam reconstruction and at the expense of increased measurement time. Grating interferometry at high energy using synchrotron sources have been already demonstrated [5]. However, access to them is limited and the operation of the interferometer is less challenging with the monochromatic radiation. Even though a proof-of-principle study of PC-CT at a laboratory source at 60 keV has been demonstrated in [6], due to very low fringe visibility of 3% the performance of the interferometer was inferior and not sufficient to perform imaging with satisfactory contrast/image quality gain between the phase and the attenuation-contrast reconstructions. Slightly different approaches have been presented to build a better performing laboratory system [7, 8], but the FOV in these cases is strongly limited.

In the following we demonstrate an X-ray phase-contrast imaging setup operating with a conventional polychromatic source that is suitable for imaging larger objects (up to 50 mm in width) and simultaneously provides the local electron density (related to the X-ray refractive index decrement) and the local X-ray attenuation coefficient distribution inside the object. We further investigate to which extent the complementarity of phase and attenuation contrast presented at low X-ray energy for low-Z materials [9] is still retained since it is lost with higher energies for low-Z materials [5].

To showcase the experimental system, an intervertebral fibrocartilage surrounded by bones was imaged and reconstructed as an example of a potential application of the technique at this photon energy range. The internal structure of the intervertebral disc shows improved contrast in the phase image and makes it possible to differentiate the fibrous capsule from the gelatinous center as previously reserved only to MR imaging.

## 2. Materials and methods

### *2.1. Grating-based X-ray phase-contrast imaging*

A detailed description and the theory of X-ray grating interferometry can be found in [10–12]. Conventional attenuation X-ray computed tomography (CT) based mainly on the photoelectric effect and Compton scattering of X-rays delivers insufficient contrast for biological tissues composed of low-Z elements. However, X-rays passing through an object are also refracted. This additional physical process can be utilized to produce a new image contrast. Unfortunately, the microradian deviations of X-rays caused by refraction in the sample are too small to be directly measured by modern state-of-the-art detectors. A different approach is therefore needed. One of them, which can be successfully used with a polychromatic spectrum produced by a labora-

#224758 - $15.00 USD Received 13 Oct 2014; revised 25 Nov 2014; accepted 7 Dec 2014; published 9 Jan 2015

tory X-ray tube [13], is a so called Talbot-Lau interferometer. It consists of three micro-periodic gratings placed between the X-ray tube and the detector. Two of them are absorption gratings (source and analyzer) typically made of gold, and the third is a phase grating made of nickel, silicon or gold. The source grating (G0) increases the coherence of the X-ray tube needed for the interference effects to occur. The phase gratings (G1) splits the incoming beam, which then interferes downstream and creates a periodic fringe pattern. The analyzer grating (G2) placed just in front of the detector transforms local fringe position into signal intensity variations.

During the CT scan, one of the gratings for each projection is moved in steps of a fraction of a period (phase-stepping) perpendicularly to the grating lines while several images are acquired. This enables the extraction of the attenuation, phase-gradient (refraction angle), and ultra-small angle scattering ("dark-field") components out of the image, thus simultaneously providing three different characteristics of the same sample. By acquiring multiple projections of the sample at different rotation angles and taking the system-specific parameters into account, the local 3D distribution of the X-ray attenuation coefficient $\mu$ (the attenuation-contrast image in the following) and the X-ray refractive index decrement $\delta$ (the phase-contrast image) can be reconstructed. The reconstruction is performed using a standard filtered back-projection with a Ram-Lak filter to reconstruct the attenuation-contrast data and a Hilbert filter to reconstruct the phase-contrast data.

### *2.2. Grating size as a limiting factor of a large field of view (FOV)*

In order to fully take advantage of the elevated X-ray energy and measure relatively large objects, bigger FOVs are necessary. In the cone-beam geometry, the size of the analyzer grating G2 placed in front of the detector is the limiting factor.

The X-ray LIGA process used for manufacturing the analyzer gratings can routinely deliver gratings up to 70 mm in diameter [14,15]. This limitation results from both the technology used for the X-ray mask membranes and from the patterning of the mask microstructures (e.g. the grating lines). With respect to the first cause, *microworks* GmbH has developed new approaches for X-ray mask membranes: a thin polyimide membrane (6 μm) replaces the established titanium membrane [16]. This allows the masks to be manufactured with diameter of 100 mm or more, and is used for direct lithographic manufacturing for gratings with thicknesses of up to 100 μm. For thicker structures, a harder X-ray spectrum is used. With such a spectrum, it is possible to use thin silicon wafers (100 μm) as mask substrates. These offer an improvement in stiffness, rigidity and thermal conductivity compared to the titanium membranes used to date. The most crucial feature is the ability to use these masks with a lithographic window of 100 mm in diameter. In order to obtain high-quality and high aspect ratio gratings, in the fist step, a polyimide-based intermediate mask is patterned using direct-write-laser lithography (DWL). It is then used to pattern structures of up to 100 μm thickness, or as in this case to fabricate using the x-ray lithography process a silicon-based working mask. This tools can then be used to manufacture gratings with thicknesses of up to 300 μm.

In the following, we present for the first time phase-contrast CT images obtained with the round analyzer grating of 10 cm in diameter. To our knowledge it is the grating interferometer with the biggest FOV reported so far. This constitutes a very significant advance towards broadening the applicability of the technique and opening a wide range of possible applications in materials science and biomedical imaging. Moreover, recent studies demonstrate the possibility of even further increased field of views by means of stitching several gratings together [17], but it has not yet been tested with gratings of such high structures ($\sim$150 μm).

#224758 - $15.00 USD Received 13 Oct 2014; revised 25 Nov 2014; accepted 7 Dec 2014; published 9 Jan 2015

### 2.3. Contrast dependence / formation

On one hand, a phase-contrast image represents the local distribution of the refractive index decrement $\delta$: [18]

$$\delta = \frac{r_0 h^2 c^2}{2\pi E^2} \sum_{i=1}^{n} N_i f_i^1, \tag{1}$$

where $r_0$ is the classical electron radius, $h$ is the Planck's constant, $c$ is the speed of light, $E$ is the X-ray photon energy, $N_i$ is the atomic density of type $i$ atoms given per unit volume, and $f_i^1$ is the real part of their atomic scattering factor in the forward direction. At X-ray photon energies far away from the absorption edges, the refractive index decrement is related to the electron density $\rho_e$ and the energy of the X-ray photons by [19]:

$$\rho_e = \frac{2\pi E^2}{r_0 h^2 c^2} \delta. \tag{2}$$

Thus, the local electron density distribution inside the sample is accessible with phase-contrast imaging.

An attenuation contrast image, on the other hand, is the result of photoelectric absorption, Compton scattering and coherent scattering in the photon energy range of interest in biomedical CT scanning [20]. Therefore, the linear attenuation coefficient $\mu$ can be decomposed into contributions from each mode of X-ray photon interaction as

$$\mu = \mu_{pe} + \mu_{coh} + \mu_{incoh}, \tag{3}$$

where *pe* is the photoelectric effect, *coh* is the coherent Raleigh scattering and *incoh* is the incoherent Compton scattering. Furthermore, the linear attenuation coefficient $\mu$ is the product of the total electronic cross section $\sigma_{\text{tot}}^e$ (cross section per electron) and the electron density of the material $\rho_e$

$$\mu = \rho_e \sigma_{\text{tot}}^e = \rho_e (\sigma_{\text{pe}} + \sigma_{\text{coh}} + \sigma_{\text{incoh}}). \tag{4}$$

Both the electronic cross sections for photoelectric effect and the coherent scattering depend not only on the photon energy $E$ but also on the material specific effective atomic number $Z_{eff}$

$$\sigma_{\text{pe}} = const \cdot \frac{Z_{eff}^k}{E^l} \tag{5}$$

and

$$\sigma_{\text{coh}} = const \cdot \frac{Z_{eff}^m}{E^n} \tag{6}$$

where values for $k$ and $m$ are typically 3.8 and 2.0, respectively, and values for $l$ and $n$ are 3.2 and 1.9, respectively, but vary slightly depending on the photon energy and on the composition of the material [20].

On the other hand, the Compton scattering cross section $\sigma_{\text{incoh}}$ depends only on the X-ray energy and is essentially independent of the atomic number $Z$ [20, 21]. Therefore, one can see that at high photon energies the linear attenuation coefficient is nearly proportional to the electron density.

As seen in Fig. 1(a), the attenuation of ethylene glycol ($C_2H_6O_2$) due to the photoelectric effect decreases with X-ray energy and becomes less than that of the Compton effect just above 26 keV. Only for X-ray energies below 26 keV is the photoelectric effect the dominant process,

#224758 - $15.00 USD Received 13 Oct 2014; revised 25 Nov 2014; accepted 7 Dec 2014; published 9 Jan 2015

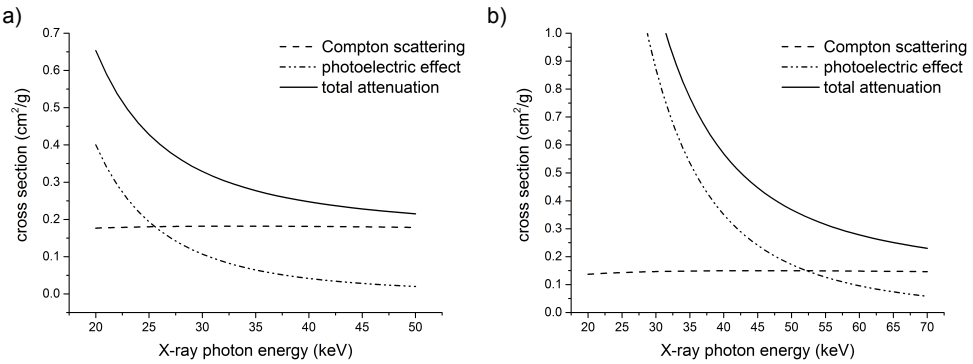


Fig. 1. Photon cross-sections calculated for ethylene glycol (a) and aluminum (b) from XCOM database [22].

and thus the biggest contribution to the attenuation contrast. The more the attenuation process results from the Compton effect, the more the attenuation-based image is proportional to the electron density, as is also the case in the phase contrast. No additional information on the material composition can be gained if attenuation is mostly attributed to Compton scattering [5]. Thus, for all low-Z materials we expect similar contrast differences for attenuation and phase contrast images at high X-ray energies. Signal-to-noise ratios and contrast-to-noise ratios will however differ and depend mainly on the performance of the grating interferometer. For instance, the higher the fringe visibility the higher these values will be in favor of phase contrast [23].

The situation changes for higher atomic number materials like aluminum (see Fig. 1(b)). At 45 keV mean X-ray energy, the attenuation contrast is a result of both effects. Therefore, attenuation- and phase-contrast images provide complementary information and materials can be more easily distinguished as seen in the monochromatic case [5].

### *2.4. Samples*

In order to experimentally investigate the discussed complementarity of phase and attenuation contrast, two different phantoms were designed. The first phantom, composed of well-defined liquids in different concentrations, was prepared to represent various low-Z materials (for the simplicity in the following called low-Z phantom). Each of the liquids was placed in a cylindrical tube made of polyethylene (PE). All of the tubes were then placed in a bigger cylindrical container filled with deionized water. The diameter of the outer container was 50 mm. Table 1 presents a list of all the liquids inside the phantom.

The second self-made phantom was made of higher-Z materials (for the simplicity in the following called high-Z phantom). Five rod-shaped materials were fixed at the top and placed in a 35 mm thick water tank during the measurements. The materials contain heavier elements with Z ranging from 9 (fluorine) to 17 (chlorine). Table 3 presents a list of all the materials inside the phantom.

Additionally, to demonstrate the capabilities of X-ray phase contrast imaging at 70 kVp, a part of a human cervical spine with intervertebral discs surrounded by bones and various soft tissue types was placed in a 40 mm diameter plastic container filled with formalin. The specimen was provided by the Institute of Forensic Medicine, Ludwig-Maximilians-Universität München (Munich, Germany) in accordance with the Declaration of Helsinki and approved by the local ethics committee.

#224758 - $15.00 USD Received 13 Oct 2014; revised 25 Nov 2014; accepted 7 Dec 2014; published 9 Jan 2015

### 2.5. Experimental setup, data acquisition and analysis

The experiments were carried out using a symmetric Talbot-Lau grating interferometer employing three gratings. It was operated at the 1st fractional Talbot order with distances between the consecutive gratings of approximately 91 cm. By having equal distances between the gratings, the highest angular sensitivity for a given system length was achieved [24]. All the gratings were produced by *microworks* GmbH, Germany. The source (G0) and the analyzer grating (G2) had periods of 10 μm and the nominal thickness of gold was approximately 150 μm. The phase grating (G1) with a period of 5 μm was made of nickel with thickness of 8 μm and gave a $\pi/2$ phase shift at the design energy of 45 keV. As an X-ray source, a COMET MXR-160HP/11 tube with a tungsten anode was used. The tube was operated at 70 kVp and 27 mA, with an effective source size of 1 mm squared. For measurements of the low-Z phantom and the biomedical sample, the emitted radiation was filtered with 60 mm of water, 2 mm of aluminum and the beryllium window of the X-ray tube resulting in an X-ray spectrum with a mean photon energy of about 45 keV, calculated by the *SpekCalc* program [25]. Mean fringe visibility of 20 % was achieved (calculated in a circular area around the middle covering half of the FOV). In the case of the high-Z phantom, 0.6 mm of copper, 2 mm of aluminum and 36 mm of water pre-filtered the beam. The resulting X-ray spectrum had a mean energy of approximately 51 keV. The change of filtering was necessary to prevent beam hardening artifacts and therefore inaccuracies in the quantitative analysis. The mean fringe visibility for this measurement was 15 %. A Varian PaxScan 2520D with a 600 μm thick structured CsI(Tl) scintillation layer and 127 μm physical pixel size served as the detector.

The samples were placed downstream of the phase grating G1 and submerged in a rectangular water tank during the experiment to avoid beam hardening and phase wrapping artifacts at the boundary between the air and the plastic containers. The distance between the sample and the phase grating and the tank thickness varied from sample to sample. The low-Z phantom and the biomedical specimen were submerged in a 60 cm thick water tank and were located at a distance about 7 cm from G1. The high-Z phantom was placed in a 36 mm thick water tank and approximately 5 cm away.

A phase stepping procedure was used in order to obtain attenuation and phase contrast images. The phase grating G1 was scanned laterally by 8 steps over one period of the interference pattern created by the grating. The phase stepping was done separately for every rotation angle of the sample. The whole CT scan consisted of 1200 rotation angles over 360 degrees and lasted approximately 10 hours. The attenuation and differential phase images were extracted by Fourier analysis [26] of the intensity oscillation curves in each detector pixel. For CT reconstruction, a GPU-based cone-beam filtered back-projection reconstruction code developed in-house based on a Ram-Lak filter for attenuation and a Hilbert filter for phase reconstruction was used. Bilateral filtering was applied to the datasets as a post-processing step, which decreased the overall noise in both reconstructions and helped to preserve the edges [27].

Both linear attenuation coefficient $\mu$ and refractive index decrement $\delta$ strongly depend on the X-ray energy. For the comparison of measured and theoretical values and for the calculation of electron densities, the effective energy of the X-ray beam has to be known. It is important to note that due to the different image formation process the measurement of $\mu$ and $\delta$ are performed at slightly different effective energies. The measured effective energy is a result of the X-ray spectrum, the spectral efficiency of the detector, and the spectral efficiency of the grating interferometer. The last one especially differs between attenuation and phase contrast. Therefore, two effective energies were defined by matching the measured and the theoretical data of a reference material. One of the materials inside each of the phantoms of known mass density and elemental weight fractions was used for this purpose. In the biological sample case, a PMMA and an epoxy resin rod were placed inside to serve as references.

#224758 - $15.00 USD Received 13 Oct 2014; revised 25 Nov 2014; accepted 7 Dec 2014; published 9 Jan 2015

Since the measurements were carried out in a water tank, the values we measure are relative to water [9]. In order to obtain the absolute values presented in Table 1 and 3, $\mu_{H2O}$ and $\delta_{H2O}$ of water for the corresponding effective energies were added to all experimental values.

For the quantitative analysis of the phantoms, 60 axial slices were averaged to increase the signal-to-noise ratio. Over each of the materials inside the phantoms, a circular region of interest (ROI) of 125 pixels in diameter was selected and the mean and standard deviations were calculated. In order to quantify image quality differences, contrast-to-noise ratios were calculated as

$$CNR = \frac{|S_a - S_b|}{\sqrt{(\sigma_a)^2 + (\sigma_b)^2}} \tag{7}$$

where $S_a$ and $S_b$ represent the measured signals, i.e., mean values in circular regions chosen for each of the materials and $\sigma_a$, $\sigma_b$ represent standard deviations of the mean for the respective regions.

As a reference for our experiments, knowing the chemical formula and the mass density of the materials, the theoretical refractive index decrement $\delta$ and linear attenuation coefficient $\mu$ values were calculated based on the adapted version of Mucal written by Bandyopadhyay and Segre [28] as described by Malecki et al. [29]. Afterwards, theoretical electron density values were calculated using Eq. (2).

## 3. Results and discussions

### 3.1. Low-Z materials phantom

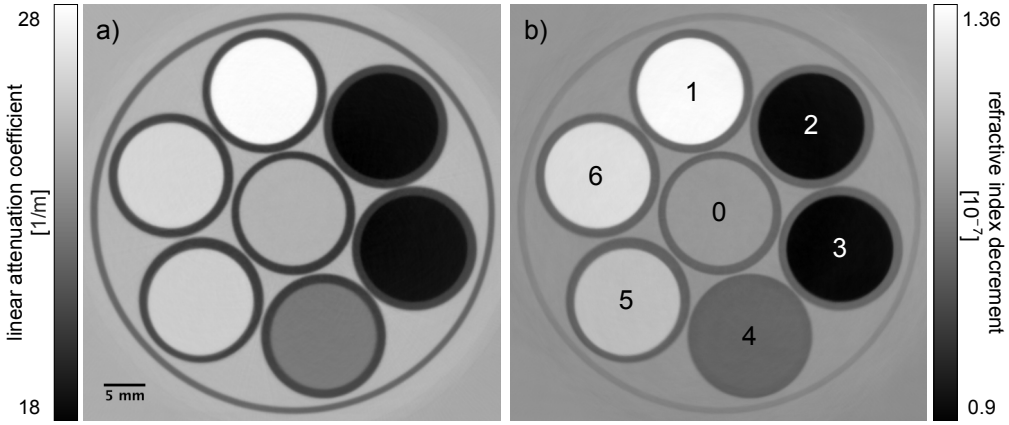


Fig. 2. Tomographic reconstruction axial slices of linear attenuation coefficient $\mu$ (a) and refraction index decrement $\delta$ (b). The liquids are as follows: 0 - water, 1 - $H_2O$/glycerol, 2 - isopropyl, 3 - ethanol, 4 - $H_2O$/ethanol, 5 - $H_2O$/ethylene glycol, 6 - ethylene glycol. Both images show a very similar contrast because of the dependence of image formation on electron density for both channels.

Figure 2 shows attenuation (a) and phase (b) contrast axial slices reconstructed from the same CT data set obtained with the Talbot-Lau interferometer. The highest signal corresponds to $H_2O$/glycerol mixture, the lowest to isopropyl alcohol. The contrast between various liquids is very similar for both images. It is due to the fact that both contrast modalities for these low-Z materials depend mainly on electron density. Dependence of attenuation contrast on material composition, namely on its effective atomic number, is greatly reduced at this X-ray energy.

The effective energy of the X-ray beam was determined by matching the measured and the calculated data for ethylene glycol. The minimum difference between measured and calculated

#224758 - $15.00 USD Received 13 Oct 2014; revised 25 Nov 2014; accepted 7 Dec 2014; published 9 Jan 2015

values was found for 44.2 keV for phase contrast and 43.7 keV for attenuation, determined with 0.1 keV resolution.

The mean values and associated standard deviations of the linear attenuation coefficient $\mu$, refraction index decrement $\delta$ and electron density $\rho_e$ together with the theoretical values are presented in Table 1. The experimental values associated with the phase-contrast reconstruction, i.e. $\delta$ and $\rho_e$, match the theoretical values within one standard deviation. In attenuation contrast, the measured values of $\mu$ show a good agreement as well but with stronger deviations from the theoretical values. The analysis is not affected by the beam hardening artifact because of the beam filtering used and because all the materials are relatively low absorbing at this energy range.

Table 1. Measured and theoretical (subscript $th$) attenuation coefficients $\mu$, refraction index decrements $\delta$ and electron densities $\rho_e$ for all fluids inside the low-Z phantom.

| Material | $\mu$ $[1/m]$ | $\mu_{th}$ $[1/m]$ | $\delta$ $[10^{-7}]$ | $\delta_{th}$ $[10^{-7}]$ | $\rho_e$ $[10^{29}/m^3]$ | $\rho_e^{th}$ $[10^{29}/m^3]$ |
|---|---|---|---|---|---|---|
| water | $25.20 \pm 0.04$ | 25.25 | $1.18 \pm 0.02$ | 1.18 | $3.35 \pm 0.03$ | 3.339 |
| $H_2O$/glycerol | $27.54 \pm 0.05$ | 27.51 | $1.35 \pm 0.02$ | 1.33 | $3.79 \pm 0.06$ | 3.739 |
| ethylene glycol | $26.10 \pm 0.04$ | 26.13 | $1.30 \pm 0.02$ | 1.30 | $3.66 \pm 0.05$ | 3.664 |
| $H_2O$/ethylene glycol | $25.94 \pm 0.04$ | 25.86 | $1.29 \pm 0.02$ | 1.27 | $3.53 \pm 0.03$ | 3.517 |
| $H_2O$/ethanol | $23.08 \pm 0.05$ | 22.98 | $1.03 \pm 0.02$ | 1.05 | $3.14 \pm 0.05$ | 3.094 |
| ethanol | $18.42 \pm 0.09$ | 18.46 | $0.955 \pm 0.02$ | 0.951 | $2.72 \pm 0.09$ | 2.684 |
| isopropyl | $18.31 \pm 0.10$ | 18.21 | $0.953 \pm 0.02$ | 0.950 | $2.71 \pm 0.04$ | 2.680 |

In order to quantify image quality difference, contrast-to-noise analysis was performed. As seen in Table 2, phase contrast provides a contrast gain over attenuation in all the cases but one. Even though both of the contrast modalities depend on the materials' electron density, phase contrast provides higher quality images because of a different image formation process and higher sensitivity of the presented technique to changes in the phase of an X-ray beam passing through an object.

Table 2. Contrast-to-noise ratios for phase contrast $CNR_{phase}$ and attenuation contrast $CNR_{abs}$ for selected sets of two materials inside the low-Z phantom.

| Material pair | $CNR_{abs}$ | $CNR_{phase}$ |
|---|---|---|
| water - $H_2O$/glycerol | 39.3 | 64.8 |
| water - $H_2O$/ethylene glycol | 13.3 | 36.8 |
| water - isopropyl | 55.0 | 53.8 |
| ethylene glycol - $H_2O$/ethylene glycol | 4.8 | 21.2 |
| ethylene glycol - $H_2O$/ethanol | 45.9 | 74.5 |
| ethylene glycol - ethanol | 69.3 | 91.3 |
| ethanol - water | 60.5 | 65.5 |
| ethanol - $H_2O$/glycerol | 82.4 | 99.8 |
| ethanol - $H_2O$/ethanol | 35.9 | 41.2 |

### *3.2. High-Z materials phantom*

The previously discussed dependence of the attenuation contrast on photoelectric absorption and Compton scattering changes with increasing Z of the material. For materials with Z ranging from 9 to 17, both effects contribute to the image formation (see Fig. 1(b)) [22].

#224758 - $15.00 USD Received 13 Oct 2014; revised 25 Nov 2014; accepted 7 Dec 2014; published 9 Jan 2015

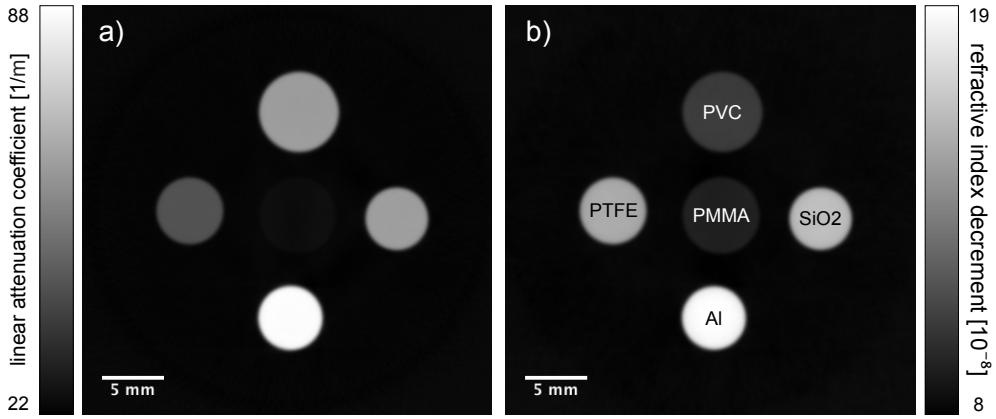


Fig. 3. Tomographic reconstruction axial slices of linear attenuation coefficient $\mu$ (a) and refraction index decrement $\delta$ (b). At 51 keV mean energy, high-Z materials show again the complementarity of both signals.

Figure 3 shows attenuation (a) and phase (b) contrast axial slices reconstructed simultaneously from the same CT data set. The highest signal corresponds to aluminum, the lowest to PMMA. The quantitative values can be found in Table 3, and CNRs for selected material pairs are presented in Table 4.

The effective energy of the X-ray beam was determined by matching the measured and the calculated data for aluminum, which gives a strong signal in both contrast reconstructions. The minimum difference between measured and calculated values was found for 52.4 keV for phase contrast and 51.8 keV for attenuation, determined with 0.1 keV resolution. The higher effective energy is an effect of stronger filtering of the beam used to prevent beam hardening artifacts and inaccuracies in the quantitative analysis. Because of the slightly different spectrum, which affects the system's fringe visibility and sensitivity, CNRs calculated for this phantom should not be directly compared to the CNRs of the low-Z phantom.

The mean values and associated standard deviations of the linear attenuation coefficient $\mu$, refractive index decrement $\delta$ and electron density $\rho_e$ are presented together with theoretical values in Table 3. Again, the experimental values of $\delta$ and $\rho_e$ match the theoretical values within one standard deviation. The measured values of $\mu$ show a good agreement with the theoretical values with maximum discrepancy of 3%. The analysis is not affected by the beam hardening because of the stronger beam filtering used.

The CNR changes depending on the respective pair of materials. For instance, between PVC and quartz a higher value of 64.8 in phase contrast compared to 14.0 in attenuation contrast could be found. The situation changes between aluminum and polytetrafluoroethylene (PTFE) for which attenuation contrast brings the ratio of 178.1 versus 28.8 in phase contrast. Contrast between PTFE and polyvinyl chloride (PVC) as well as water and PTFE is similar for both images. Clearly, complementary information looking at the phase- and attenuation-contrast images is accessible in the case of these materials with higher atomic numbers.

### *3.3. Intervertebral discs*

An intervertebral disc consists of two regions, i.e., the nucleus pulposus and the surrounding annulus fibrosus. The inner nucleus pulposus is a visco-elastic gel composed of a disordered network of type-II collagen fibrils. The outer annulus fibrosus is made of highly organized and densely packed type-I collagen whose fibers run parallel to each other [30].

#224758 - $15.00 USD Received 13 Oct 2014; revised 25 Nov 2014; accepted 7 Dec 2014; published 9 Jan 2015

Table 3. Measured and theoretical (subscript $th$) attenuation coefficients $\mu$, refraction index decrements $\delta$ and electron densities $\rho_e$ for all the materials inside the high-Z phantom.

| Material | $\mu$ $[1/m]$ | $\mu_{th}$ $[1/m]$ | $\delta$ $[10^{-7}]$ | $\delta_{th}$ $[10^{-7}]$ | $\rho_e$ $[10^{29}/m^3]$ | $\rho_e^{th}$ $[10^{29}/m^3]$ |
|---|---|---|---|---|---|---|
| water | $23.16 \pm 0.18$ | 22.72 | $0.839 \pm 0.005$ | 0.838 | $3.334 \pm 0.02$ | 3.339 |
| PVC | $60.82 \pm 0.19$ | 59.14 | $1.08 \pm 0.03$ | 1.08 | $4.304 \pm 0.01$ | 4.320 |
| PTFE | $45.49 \pm 0.11$ | 46.51 | $1.59 \pm 0.06$ | 1.60 | $6.350 \pm 0.02$ | 6.363 |
| aluminum | $89.29 \pm 0.22$ | 89.29 | $1.97 \pm 0.04$ | 1.97 | $7.848 \pm 0.05$ | 7.843 |
| $SiO_2$ | $64.15 \pm 0.14$ | 65.83 | $1.69 \pm 0.04$ | 1.66 | $6.728 \pm 0.04$ | 6.620 |
| PMMA | $25.07 \pm 0.43$ | 24.68 | $0.969 \pm 0.003$ | 0.971 | $3.860 \pm 0.01$ | 3.868 |

Table 4. Contrast-to-noise ratios for phase contrast $CNR_{phase}$ and attenuation contrast $CNR_{abs}$ for selected sets of two materials inside the high-Z phantom.

| Material pair | $CNR_{abs}$ | $CNR_{phase}$ |
|---|---|---|
| water - PMMA | 4.1 | 22.0 |
| water - PTFE | 102.4 | 96.1 |
| water - PVC | 144.3 | 41.8 |
| PVC - $SiO_2$ | 14.0 | 64.8 |
| PVC - aluminum | 97.9 | 73.7 |
| PTFE - aluminum | 178.1 | 28.8 |
| PTFE - PMMA | 46.5 | 91.4 |
| PTFE - PVC | 69.5 | 76.9 |

Figure 4 shows reconstruction slices of an intervertebral disc surrounded by vertebral bodies and various adjacent soft tissue types. Because of the X-ray energy used, the bone does not obstruct the surrounding soft tissue with strong artifacts and its internal structure can be reconstructed. The biggest improvement of the phase-contrast reconstruction (Fig. 4(b) and (d)) over the conventional attenuation reconstruction (Fig. 4(a) and (c)) is greatly increased visibility of the boundary between the disc annulus and nucleus pulposus inside the intervertebral disc (indicated by the arrows). This is a very interesting finding, as normally it is a feature expected to be seen only in MR imaging, not in X-ray CT.

Collagen is a low-Z material and hence one should not expect a big difference in its visibility between the two imaging contrasts/modalities. However, as previously mentioned it is very dense and organized differently depending on the region. We believe that this and the fact that at the mean X-ray energy of the measurement the attenuation contrast image seems to not be completely dominated by the Compton effect are the reasons for the increased visibility of the boundary in the phase-contrast reconstruction. In addition, there is more anatomical information in the phase-contrast image compared to the attenuation image because of slightly increased contrast between the formalin and the soft tissue surrounding the bones.

The effective energy of the X-ray beam was determined by matching the measured and the calculated data for PMMA. The minimum difference between measured and calculated values was found for 43.5 keV for phase contrast and 42.9 keV for attenuation.

In order to quantify the contrast enhancement between the phase and the attenuation reconstructions, four regions of interest (ROIs) were selected and CNRs calculated. The ROI selection is indicated by squares in Fig. 4(b). Between ROI1 and ROI2 (15x15 pixels) a higher value of 16.9 in phase contrast compared to 6.9 in attenuation contrast could be found. The same situation is present between ROI3 and ROI4 (25x25 pixels) for which phase contrast brings the

#224758 - $15.00 USD Received 13 Oct 2014; revised 25 Nov 2014; accepted 7 Dec 2014; published 9 Jan 2015

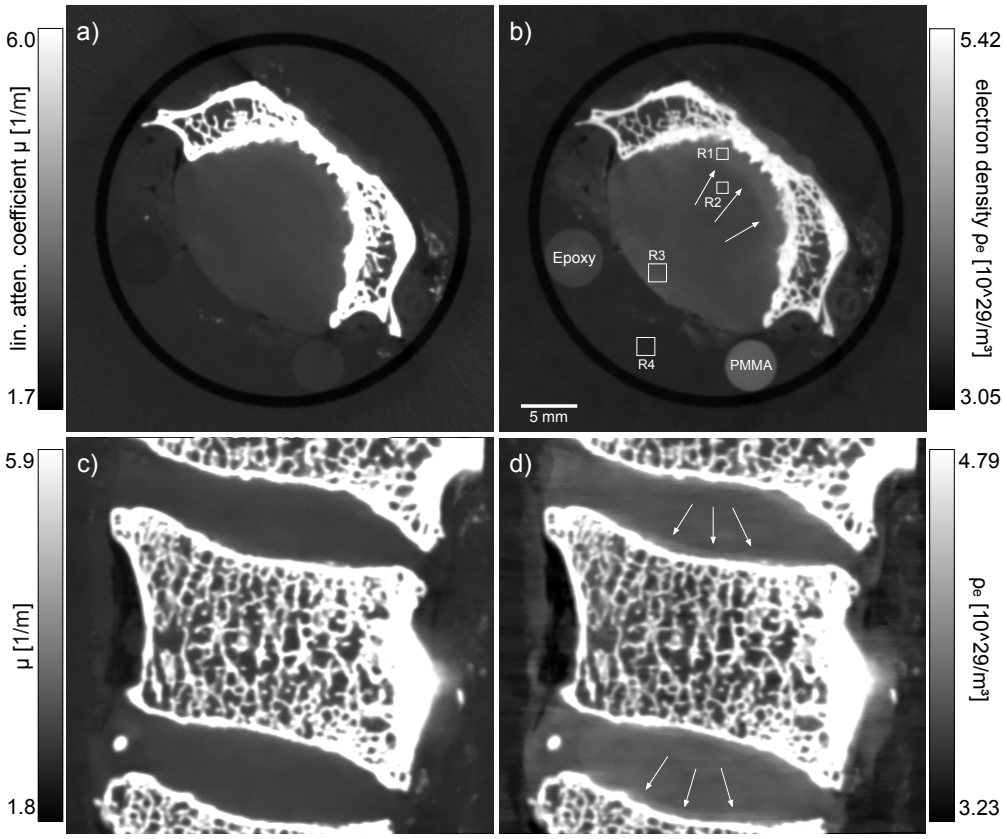


Fig. 4. Tomographic reconstruction slices of the human cervical spine. Phase-contrast axial (b) and sagittal slice (d) show improved visibility of the intervertebral discs over attenuation-contrast axial (a) and sagittal slice (c). Internal structure of the discs is visible and the clear boundary between the disc annulus and the nucleus pulposus can only be seen in the phase-contrast image (indicated by the arrows).

ratio of 7.6 versus 3.4 in attenuation contrast.

## 4. Conclusions

In conclusion, we demonstrated for the first time the feasibility of quantitative high-energy X-ray phase-contrast CT using a Talbot-Lau interferometer with a polychromatic X-ray source and a 10 cm round analyzer grating. In particular, we have shown that the system used simultaneously provides quantitative information on the local 3D distribution of the linear attenuation coefficient $\mu$, refraction index decrement $\delta$ and the electron density. As a result of the increased field of view, ours is the first grating-based X-ray phase-contrast CT setup for samples up to 50 mm in width. We believe that imaging of cartilage surrounded by bones is one of the most promising biomedical applications.

Tomography scans of two phantoms were performed in order to quantitatively assess information on material properties and to investigate contrast dependence of phase and attenuation images for materials of various atomic numbers. In both cases, the refraction index decrements $\delta$ and electron densities $\rho_e$ agree very well with the theoretical values within one standard deviation. The measured linear attenuation coefficients $\mu$ agree well with a maximum discrepancy

#224758 - $15.00 USD Received 13 Oct 2014; revised 25 Nov 2014; accepted 7 Dec 2014; published 9 Jan 2015

of 3%. The stronger deviations may be associated with higher noise in the attenuation contrast due to the scattering. Further investigations concerning this issue are needed. Since $\mu$ values deviate stronger it is harder to distinguish the materials in the attenuation-contrast image than in the phase-contrast image.

For low-Z materials both attenuation- and phase-contrast images contain the same information on various materials. Due to the domination of X-ray attenuation by Compton scattering, the same physical information (i.e. the electron density) is represented in both contrast modalities. However, the experimental setup has been successfully designed to provide enhanced, in the form of higher contrast-to-noise ratios, phase-contrast images as compared to the attenuation-contrast results, hereby confirming the experimental findings from the monochromatic case by Willner et al. [5]. This contrast gain depends strongly on the specific grating interferometer and its optical parameters. Therefore, one has to remember that the presented setup is in a research phase and could be further improved by optimizing its parameters. The fringe visibility, which strongly dictates the system's performance [23,31], could be more than doubled by increasing the absorption grating structures' height or by inclining the gratings with respect to the axis of the X-ray beam [32]. Also the angular sensitivity could be increased by making the grating periods smaller while keeping the system length constant [7]. Moreover, filtering the parts of the spectrum which reduce the overall fringe visibility would increase the system capabilities. Only when optimized for the optimum optical performance, i.e. having both high visibility and high angular sensitivity, could clinically dose-compatible applications be foreseen [7].

The most promising but not yet explored field for the presented effective X-ray energy around 45 keV are materials science applications. High penetration depth allows investigation of dense and big objects. As seen from the results of the second phantom, the possibility to simultaneously access various information on material composition provides added value over attenuation-only-based images.

The authors strongly believe that the demonstration of quantitative high-energy X-ray phase-contrast CT working with a conventional X-ray tube is an important step in opening a broad range of applications for the technique such as biomedical imaging, materials science, and other research areas.

**Acknowledgments**

The authors would like to thank Andreas Fehringer for providing the GPU-based cone-beam CT reconstruction tool, Sebastian Allner for using his implementation of bilateral filter on the biological sample reconstruction, Juliana Martins for helping with preparation of the liquids for the low-Z phantom, and Richard Clare for proofreading the manuscript.

Research was conducted with financial support by the DFG Cluster of Excellence Munich-Centre for Advanced Photonics (MAP), the DFG Gottfried Wilhelm Leibniz program and the European Research Council (ERC, FP7, StG 240142). This work has been partly funded by the Bayerisches Staatsministerium für Wirtschaft, Infrastruktur, Verkehr und Technologie under contract number 13 30 / 89265 / 5 / 12. This work was carried out with the support of the Karlsruhe Nano Micro Facility (KNMF, www.kit.edu/knmf), a Helmholtz Research Infrastructure at Karlsruhe Institute of Technology (KIT).

#224758 - $15.00 USD Received 13 Oct 2014; revised 25 Nov 2014; accepted 7 Dec 2014; published 9 Jan 2015